Optics & Laser Technology 176 (2024) 111029

Contents lists available at ScienceDirect

Optics and Laser Technology

journal homepage: www.elsevier.com/locate/optlastec

Full length article

Optical vortices by an adaptive spiral phase plate

T. Jankowski [a], N. Bennis [a], P. Morawiak [a], D.C. Zografopoulos [b], A. Pakuła [c,a], M. Filipiak [d], M. Słowikowski [d], J.M. López-Higuera [e,f,g], J.F. Algorri [e,f,g,*]

[a] Faculty of Advanced Technologies and Chemistry, Military University of Technology, Warsaw 00-908, Poland
[b] Consiglio Nazionale delle Ricerche, Istituto per la Microelettronica e Microsistemi (CNR-IMM), Rome 00133, Italy
[c] Faculty of Mechatronics, Warsaw University of Technology, Św. Andrzeja Boboli 8 02-525 Warsaw, Poland
[d] The Centre for Advanced Materials and Technologies CEZAMAT, Warsaw University of Technology, 19 Poleczki St. 02-822 Warsaw, Poland
[e] Photonics Engineering Group, University of Cantabria, 39005 Santander, Spain
[f] CIBER de Bioingenierí a, Biomateriales y Nanomedicina, Instituto de Salud Carlos III, 28029 Madrid, Spain
[g] Instituto de Investigación Sanitaria Valdecilla (IDIVAL), 39011 Santander, Spain

ARTICLE INFO

Keywords:
Optical vortices
Liquid crystals
Orbital angular momentum

ABSTRACT

An Adaptive Spiral Phase Plate (ASPP) based on liquid crystal (LC) and the transmission electrode technique is theoretically and experimentally demonstrated. This ASPP design enables the generation of high-quality optical vortices with topological charges ranging from ±1 to ±4 using a single device, with higher charges being directly achievable by employing higher-birefringence LC or thicker cells. The continuous reconfigurability of the optical phase shift, achieved through a simple control mechanism involving only two low voltages and 100 electrodes that distribute the voltage, sets this device as an accurate approximation to a continuous ASPP. The measured conversion efficiency ranges between almost 100% and 95% for the first and fourth topological charges, respectively. This device offers remarkable advantages, such as complete reconfigurability, allowing adjustment of operating wavelengths and topological charges. The fabrication process mirrors that of a standard LCD cell, ensuring a cost-effective and reliable solution. In summary, the proposed ASPP is a key advancement, providing superior light conversion efficiency, simplicity, and the capability for on-the-fly reconfiguration in various optical applications.

1. Introduction

Over the last decade, helical wavefronts have been amongst the most extensively studied complex phase-shapes of light. They are characterised by an azimuthal phase dependence of $e^{-il\Phi}$, where l is a variable that represents the topological charge of the vortex, which determines how many times the phase of the wavefront wraps around in 360°, and Φ is the azimuthal angle in polar coordinates, which measures the angle in the plane perpendicular to the direction of propagation of the light beam. When focused, these light beams carry an orbital angular momentum (OAM) that forms rings rather than points in a focal plane. The potential and applications of this phenomenon have seen an exponential rise with use-cases ranging from laser processing [1–3], beam shaping [4], optical tweezers [5], atom manipulation [6] and free-space communications [7]. The last decade also witnessed rapid advancements in optical vortices and OAM applications. In 2013, terabit-level optical communication was demonstrated via OAM multiplexing in fibres [8]. In 2016, Ref. [9] demonstrated the generation of extreme OAM states exceeding 10.000$\hbar$ and accomplished quantum entanglement of these states. In the following three years, a plethora of tunable properties of optical vortices have been skillfully managed at the nanoscale. These include the conversion of spin angular momentum to OAM for classical [10] and quantum light [11], tunable wavelengths ranging from visible light [12,13] to X-ray light [14], ultra-broadband tunable OAM [15], adaptable chirality [16] and time-varying OAM in extreme-ultraviolet vortex beams [17]. Also, the vortex beam enables the transfer of OAM to particles, producing rotation and translation [18,19]. Other remarkable applications have been high optical power lenses [20] or advanced microprinting technology [21].

Traditionally, optical vortices are generated using spiral phase plates (SPPs) [22] or computer-generated holograms (CGHs) [23]. SPPs have been produced using a variety of techniques, such as multi-stage vapour deposition processes or direct electron-beam writing and, more recently, metasurfaces [24]. In these cases, the helical surface is discretised into different steps of refractive index. A fixed SPP is obtained by matching the refractive index to that of an azimuthal phase dependence. For CGHs, they generate a spiral interference fringe.

* Corresponding author at: Photonics Engineering Group, University of Cantabria, 39005 Santander, Spain.
E-mail address: algorrijf@unican.es (J.F. Algorri).

https://doi.org/10.1016/j.optlastec.2024.111029
Received 14 December 2023; Received in revised form 22 March 2024; Accepted 13 April 2024
Available online 20 April 2024

The number of spiral arms and their rotation direction represent the number and sign of the topological charge. These distinct interference patterns are commonly used to determine the topological charge of a vortex beam [24]. Leveraging the characteristics of this interference, a hologram plate can be created from either the spiral fringe or the fork grating [25]. Blazed forked gratings have been instrumental in concentrating more energy in the first diffraction order [25]. However, fabricating CGHs remains a challenge. The use of SPPs also faces drawbacks due to fabrication limitations and a lack of reconfigurability, leading to fixed topological charges and operating wavelengths. Recent years have seen attempts to resolve these issues through alternatives like spatial light modulators (SLMs) [26]. This structure results in two outcomes. Firstly, the portion of the incoming intensity that is transmitted or reflected is determined by the fill factor, which is inversely proportional to the pixel interspacing. Secondly, the primary central diffraction order has an intensity fraction that is proportional to the square of the fill factor, while the remaining intensity is dispersed among other higher diffraction orders. The result is an efficiency around 60%–85% range [27], and poor fill factors <40% [28]. Another option is to use liquid crystal (LC) and individual pie slices of indium tin oxide (ITO) as contact electrodes, resulting in a discretised SPP. The first version used 16 electrodes to produce $l = 2$ and $l = 1$ [29], and the next proposal obtained 8 topological charges by stacking several LC cells but at the cost of reducing efficiency [29,30]. Several years later, the use of spiral-shaped electrodes was proposed, resulting from combining an SPP with the phase of a diffractive lens [31]. The result is a Spiral Diffractive Lens (SDL) that generates different topological charges (ml) and focal lengths (f/m) corresponding to the different diffractive harmonic orders (m). The result is that several vortices can be found in a single beam. After that, this design has been improved by using more electrodes of control (e.g. 24 electrodes, up to $l = 12$ [32,33], a comprehensive review can be found in Ref. [28]). Yet, these solutions present their own set of challenges, such as complex voltage control, light efficiency loss and complications due to the need to combine the phase pattern with a blazed grating pattern.

One way to compare different technologies is through their conversion efficiency. In the field of optical vortex generators, this term is often used alongside the terms diffraction efficiency and transmission efficiency. For instance, in the context of metasurfaces, it is used to describe the proportion of the input power that successfully passes through the device. This term is also referred to as transmission efficiency and primarily depends on the mismatch with the free-space impedance, leading to back-reflection of the incident power and, to a lesser degree, the material absorption losses. For example, a TiO_2 metasurface has a conversion efficiency of around 60% at 532 nm [34], indicating that 60% of the input power is transmitted through the device. In the case of Silicon, the use of cylindrical nanodisks enables a transmission efficiency of more than 70% [35]. On the other hand, in the context of diffractive generators, conversion efficiency is also referred to as diffraction efficiency. It is important to note that typically in optics, diffraction efficiency is defined as the ratio of the optical power, of a given order, to the total incident light [36], while in the field of optical vortex generators usually refers to the ratio of the optical power, of a given order, to the total transmitted light [37]. In order to avoid confusion, we will define absolute diffraction efficiency for the first case and relative diffraction efficiency for the second one. For CGHs first attempts to fabricate them produced very low efficiencies, e.g. in silica glass by femtosecond laser pulses in the order of 5% (absolute) [38], recorded in a cell filled with polymer-dispersed liquid crystal material 13%–17% (relative) [39], using an LC cell where one electrode was patterned with a computer-generated hologram 27% (relative) [40] or using a blue phase LC fork grating by applying a vertical electric field with a forked electrode 33% (relative) [41]. In addition to the low efficiencies, the previous methods have fixed patterns or electrodes, so changing the topological charge is impossible. One option is to use SLM, but as previously commented, they have serious drawbacks. Recently, photopatterning has been proposed on a Digital Micro-mirror Device (DMD)-based microlithography system, with single conversion efficiency up to 37.5% (absolute) [42]. In the case of SPP generators based on pie slices, the first studies defined the conversion efficiency as the ratio of the optical power in zero diffraction order to the total transmitted light (like a relative diffraction efficiency). As expected, very high values were demonstrated for topological charges 1 and 2 (in the order of 100%) [29] and 55% for 8 [30]. In addition, it should be considered that there are losses mainly caused by the interface reflections between air-glass and glass-LC and scattering at the ITO electrode gaps (and to a lesser extent due to LC scattering) [30]. This loss can be in the order of 10%–15% [30].

The present study introduces a breakthrough structure employing LC and the transmission electrode technique. Previous research has showcased the application of this method in spatial phase modulation of several types [43,44] and in various kinds of LC lenses, e.g., cylindrical and Powell [45,46], axicons [43,47,48], aspherical [49–53] and arrays [54]. In this scenario, it is feasible to attain a continuous spiral voltage profile by leveraging a variation of the transmission electrode technique. This innovative structure can generate an almost continuous spiral phase profile (100 electrodes distribute the voltage) that is completely reconfigurable using only two low voltages. This novel adaptive spiral phase plate (ASPP) has the potential to generate various positive and negative topological charges (up to $l = \pm 4$ are here experimentally demonstrated with a low birefringence LC), reducing complexity and enhancing efficiency in applications, such as optical tweezers or OAM mode division multiplexing, paving the way for the next wave of advancements in the exciting field of optical vortices.

2. Structure and operation principle

The device comprises a pair of substrates, each coated with ITO. Only one substrate is photolithographed using the transmission electrode pattern. Fig. 1(a) illustrates a schematic of the overall structure. The substrates are separated by a 50-μm thick spacer. The cavity formed in between is occupied by the nematic LC 6-CHBT, with a birefringence $\Delta n = 0.16$, dielectric permittivity $\Delta\epsilon = 7$ [55] and elastic constants $K_{11} = 6.71$ pN (splay), $K_{22} = 2.93$ pN (twist), and $K_{33} = 6.1$ pN (bend) [56]. The device is designed as an adaptive phase-only modulator and does not require a molecular twist. Hence, homogeneous alignment is achieved through a rubbing process. This is achieved by utilising a polyimide alignment layer (Nissan SE-130), rubbed parallel to the electrodes for the upper glass and in the opposite direction for the lower one.

The operational principle of the device is straightforward. The key component is a circular transmission electrode (radius $r = 1$ cm) that generates a continuous voltage profile from one electric contact to the other, the grey square pads of Fig. 1(b). In this case, an electrode width (w) of 10 μm is chosen for the transmission electrode. The voltage values V_1 and V_2 represent the applied voltage on the top electrodes. Subsequently, a series of ITO pie slices ($N = 100$ slices in this case) that extend from the periphery to the centre distributes the voltage throughout the active area, see Fig. 1(c). Note that drawings are not to scale, the actual gap between slices is $g = 10$ μm. The broader part of the slices has $2\pi r/100 - g = 618$ μm, whereas it ends on a spike. One of the advantages of the transmission electrode technique is that the resistance from V_1 to V_2 is very high. Considering the sheet resistance ($R_{sq} = 100$ Ω/sq) and ITO thickness ($t = 20$ nm), the theoretical resistance (based on numerical simulations) is $R = 66.4$ kΩ. For example, for gradient voltages of 1 V_{RMS} it implies a current of only 15 μA_{RMS}. On the other hand, one challenge of this configuration is that a certain central area is unused due to the gap between slices. Specifically, a circumference with a radius $r = Ng/2\pi = 159$ μm. As observed in the simulations and experimental results, this region is very small compared to the active area. Moreover, it could be considerably reduced by improving the resolution of the photolithography. For

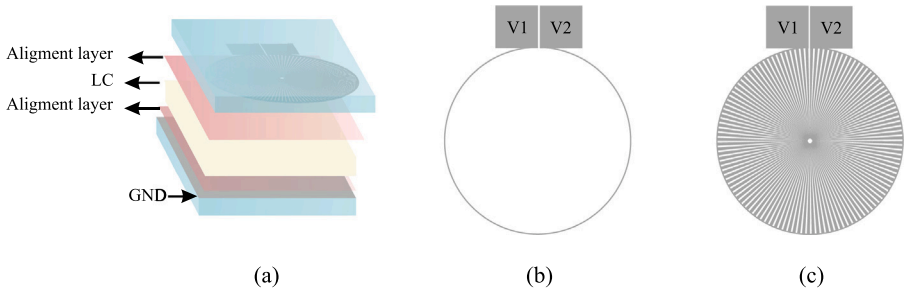

Fig. 1. (a) Schematic depiction of the LC-tunable optical vortex generator and its various constituent parts. (b) Schematic depiction of the circular transmission electrode alone and (c) including the ITO slices evenly arranged to distribute the voltage. Note these drawings are not to scale (the space between adjacent slices is only 10 μm).

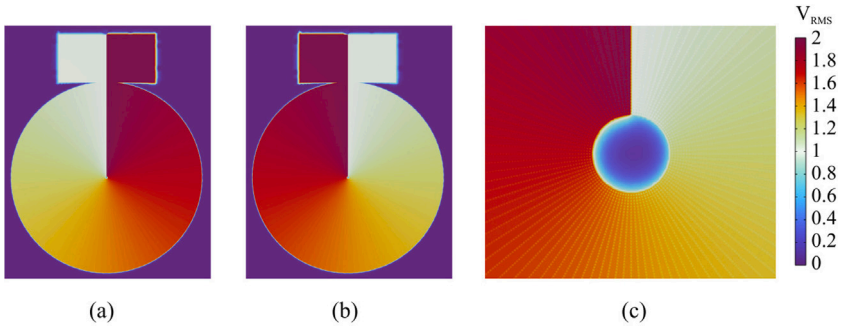

Fig. 2. Voltage profile in the transmission electrode layer for (a) $V_1 = 1$ V_{RMS}, $V_2 = 2$ V_{RMS} (1 kHz) and (b) $V_1 = 2$ V_{RMS}, $V_2 = 1$ V_{RMS} (1 kHz). (c) Zoom of the central area.

example, a 1 μm resolution photolithography would produce only a 15.9 μm singularity region that, being considerably lower than the thickness, would lead to a low voltage/phase step, as demonstrated below.

The total voltage distribution is numerically calculated by numerical methods considering a static approach of the LC (constant dielectric anisotropy, ϵ_o and ϵ_e) and the whole structure. The results of Fig. 2(a), corresponding to the voltage at the upper electrode plane for an AC signal of 1 kHz with $V_1 = 2$ V_{RMS} and $V_2 = 1$ V_{RMS} demonstrate a voltage distribution that has a homogeneous transition in the active area. As seen in Fig. 2(b), the use of inverted voltages in V_1 and V_2 demonstrates the possible use in generating both positive and negative topological charges. Finally, as can be seen in Fig. 2(c), a central region remains uncovered with ITO due to the gap between slices, in this case, a circumference of 320 μm, which produces a voltage gap at the centre with the voltage dropping to zero. This defect area is located in the centre of the ASPP, where the electric field is zero in the generated AOM modes, hence its influence is negligible. On the other hand, the effect of the gap between slices (10 μm) also produces a slight voltage drop in this region, but considerably lower than the previous effect. The lines around the central gap observed in Fig. 2(c) reveal a maximum drop of 5 mV_{RMS}. Consequently, this effect should not be noticeable for LC with low birefringence and devices with low thickness (the phase step will not be high).

The linearity of this electrical field distribution is key to maintaining a perfect vortex generator. However, the LC birefringence curve is non-linear, so this issue has to be carefully taken into account. A simulation of the LC birefringence response as a function of voltage (taking into account the 6-CHBT elastic constants and Frank-Oseen equations [57]) is presented in Fig. 3. The axis on the right represents the phase shift considering that the phase equals $\phi = \Delta n d/\lambda(2\pi)$ rad, the LC thickness is $d = 50$ μm and $\lambda = 632.8$ nm. Traditionally, two characteristic regions in this curve have to be avoided. The first one is produced when the electrical energy overcomes the elastic free energy and the molecules start to move (just above the threshold voltage, V_{th}). The other one is produced when the molecules start to reach the perpendicular position (at the saturation voltage, V_{sat}). In this case, the range from V_{th} to V_{sat}

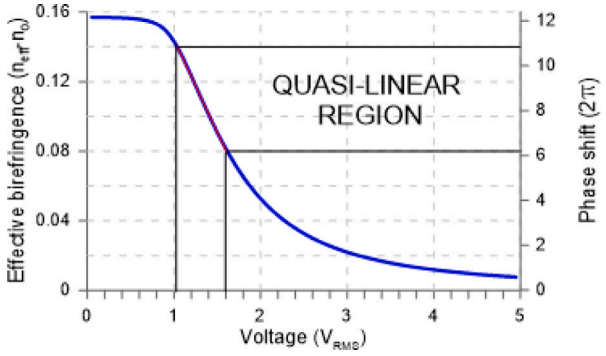

Fig. 3. Characteristic birefringence curve as a function of voltage for the nematic 6-CHBT.

is around 0.9 V_{RMS} to 3 V_{RMS}, respectively. Close to these two values, the birefringence still has a high non-linearity. Hence, a considerable margin has to be considered in order to operate in a quasi-linear region, in this case from 1 V_{RMS} to 1.6 V_{RMS}. As a linear phase profile characterises an ideal SPP, this operating range has to be maintained. Considering this range (effective birefringence $\Delta n = 0.14–0.08 = 0.06$), the maximum linear phase shift is 4.74 (2π) rad, corresponding to a maximum theoretical topological charge of $l = 4$.

3. Setup and experimental results

The optical system shown in Fig. 4 is used to simultaneously measure the azimuthal change of the optical phase retardation characteristic of ASPP and the generated optical vortex beam. The light source for this system is an expanded and collimated laser beam with a wavelength of 632.8 nm. A non-polarising beam splitter (NPBS) is placed after the ASPP to divide the beam into two paths. One of these paths, reflected by the NPBS, is used to ensure the correct selection of the applied voltages (V_1 and V_2).

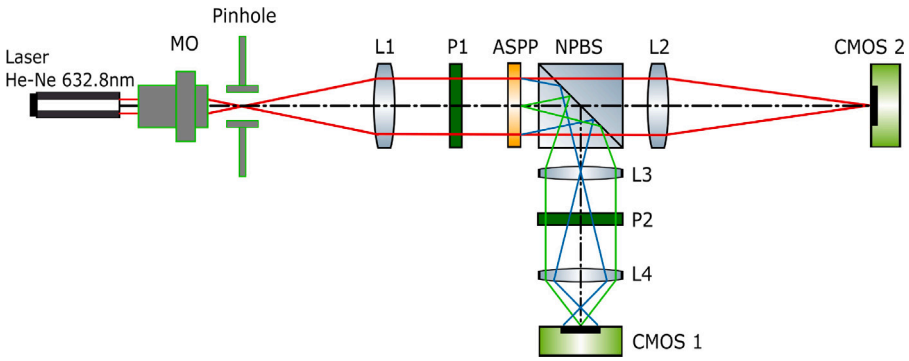

Fig. 4. Schematic of the optical system for measuring simultaneously the azimuthal change of phase retardation and the generated optical vortex beam of the ASPP.

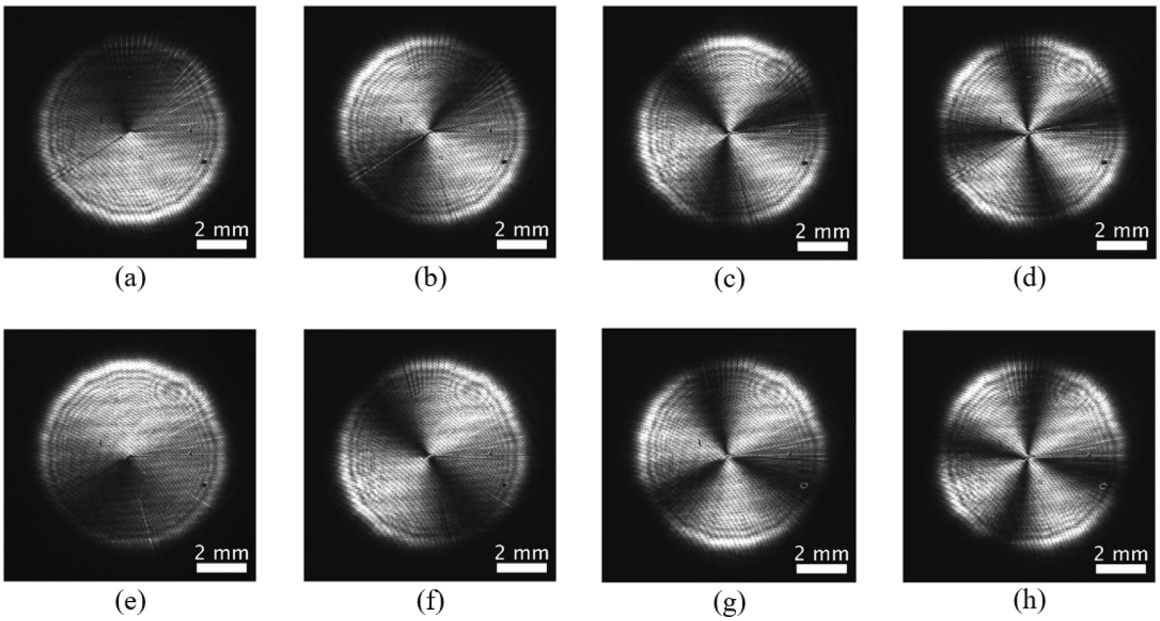

Fig. 5. Phase shift for different topological charges (a) $l = 1$, $V_1 = 1.6$ V_{RMS}, $V_2 = 1.46$ V_{RMS}, (b) $l = 2$, $V_1 = 1.6$ V_{RMS}, $V_2 = 1.34$ V_{RMS}, (c) $l = 3$, $V_1 = 1.61$ V_{RMS}, $V_2 = 1.24$ V_{RMS}, (d) $l = 4$, $V_1 = 1.61$ V_{RMS}, $V_2 = 1.14$ V_{RMS}. (e)–(h) For $l = -1$ to $l = -4$ the inverted voltages in V_1 and V_2 are applied.

This beam is directed onto the ASSP, which is positioned between two linear crossed polarisers (P1 and P2). These polarisers are oriented at +45° and −45° with respect to the LC optical axis, respectively. This setup allows for measuring the interference pattern between extraordinary and ordinary rays. The image of the ASPP is adapted onto the CMOS 1 camera (BASLER acA2500–60μm) using two bi-convex lenses (L3, L4). From the data captured by this camera, the topological charge can be calculated by observing the bright-dark transitions (each transition corresponds to a 2π radian change). The other path, transmitted through the NPBS, is focused by the lens L2 onto the CMOS 2 camera (FLIR CM3-U3-13S2C-CS). This camera is located at the focal plane of the L2 lens. This configuration allows for capturing the optical vortex beam at the focal plane of the lens when the polariser P1 is parallel to the rubbing direction of the ASPP. When a light beam passes through a polariser whose polarisation axis is parallel to the LC optical axis, the light is affected by the effective refractive index of the molecules.

The results of the phase shift distribution can be observed in Fig. 5. The LC layer has the ability to generate eight distinct topological charges, specifically from $l = \pm1$ to ±4. As it was predicted in the birefringence study, minor alterations in the applied voltage can lead to substantial modifications in phase shifts. It is important to note that 2π multiples are necessary for the formation of optical vortices. Additionally, by minutely adjusting the applied voltage, the phase shift can be sustained at 2π (or a multiple thereof). In our case, to obtain perfect linear phase profiles one voltage is fixed around 1.6 V_{RMS} and the other shifts from 1.46 V_{RMS} (gradient of 0.14 V_{RMS} for $l = \pm1$) to 1.14 V_{RMS} (gradient of 0.47 V_{RMS} for $l = \pm4$).

A phase unwrapping procedure is carried out to demonstrate the linearity of the phase profile. The phase profile analysis was conducted through a series of steps. A median filter was initially applied to the raw images utilising a 15 × 15 pixel window. Subsequently, the weighted median angular intensity was computed at eight distinct radii, ranging from 100 to 450 pixels, with 1000 points along the circle, Fig. 6(a)–(d). The weight of the smaller circles was scaled down according to their radii. To ensure that the start and end points of the fitted curve matched the raw data, weights were added to the fit for the spline fitting of the intensity. This was crucial to ensure that we returned to the same intensity after traversing through all 360°. Following this, peak-to-peak normalisation of the intensities was performed. This step was necessary as the phase between maximum and minimum intensity had to be π for higher topological charges, and it facilitated the phase approximation.

As can be observed, for higher topological charges, there is a slight deviation from applying positive voltage gradient or negative voltage gradients (the absolute intensity signal is not perfectly inverted). This can be caused by some impurities at the LC, producing an undesired accumulation of ions and some hysteresis. Despite this, this effect does not affect the relative phase profiles, as shown below.

Lastly, the phase change between 0 and 360° in that line was calculated following the Jones Matrix formalism. Specifically, it has

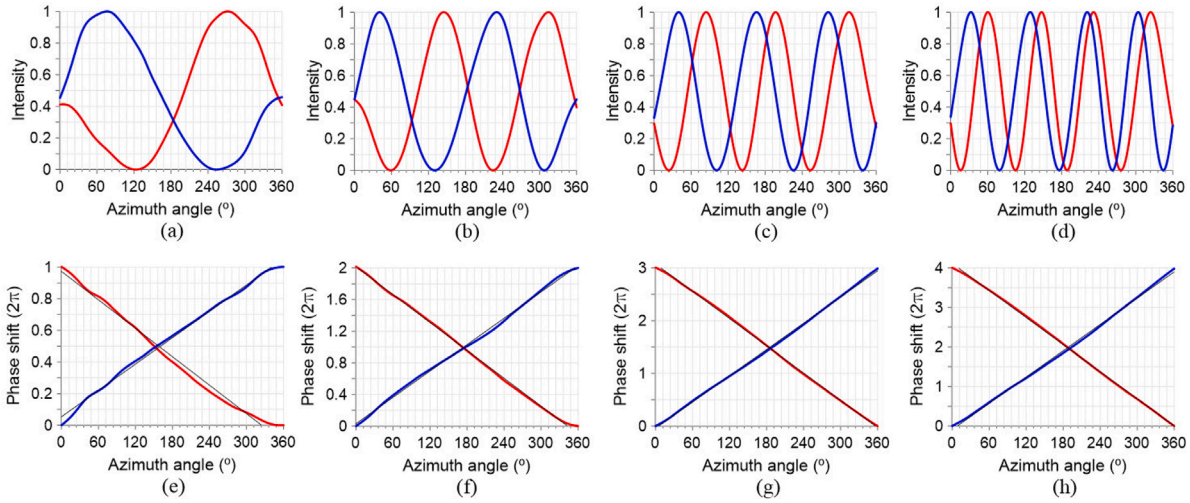

Fig. 6. (a)–(d) Intensity and (e)–(h) phase shift profiles for different topological charges. The applied voltages are (a), (e) $l = \pm 1$, $V_1 = 1.6$ V_{RMS}, $V_2 = 1.46$ V_{RMS}, inverted voltages in red, (b), (f) $l = \pm 2$, $V_1 = 1.6$ V_{RMS}, $V_2 = 1.14$ V_{RMS}, inverted voltages in red, (c), (g) $l = \pm 3$, $V_1 = 1.61$ V_{RMS}, $V_2 = 1.24$ V_{RMS}, inverted voltages in red, (d), (h) $l = \pm 4$, $V_1 = 1.61$ V_{RMS}, $V_2 = 1.24$ V_{RMS} inverted voltages in red.

to be taken into account that the vertical polarisation component is affected by the LC device and the radial linear phase deviates this component towards the beam axis. On the contrary, the horizontal linear polarisation component is unaffected and remains collimated. Thus, except for a constant phase term, the Jones matrix describing the ASPP can be written as Eq. (1).

$$M_{\mathrm{ASPP}}(r) = \begin{bmatrix} 1 & 0 \\ 0 & \exp[i\phi(r)] \end{bmatrix}, \tag{1}$$

where ϕ(r) is the radially dependent retardation which, ideally, should be linear with r as $\phi(r) = k_r^{\mathrm{ASPP}} r$ being k_r^{ASPP} the radial wavenumber imparted by the ASPP device. Now, considering a second polariser (P2) oriented at 45° behind the ASPP, the two polarisation components interfere and the Jones vector after the polariser reads

$$Jout(r) = \frac{1}{\sqrt{2}} \begin{bmatrix} 1 & 1 \\ 1 & 1 \end{bmatrix} \cdot M_{\mathrm{ASPP}}(r) \cdot \frac{1}{\sqrt{2}} \begin{bmatrix} 1 & 1 \end{bmatrix}^T = \frac{1}{2} \{1 + exp[\phi(r)]\} \begin{bmatrix} 1 \\ 1 \end{bmatrix}, \tag{2}$$

where the first term corresponds to the Jones matrix of the second polariser and the third to the normalised Jones vector standing for the input beam (T indicating the transpose vector). Considering this, the output field intensity is given by

$$I(r) = J_{\mathrm{out}}^{\dagger} \cdot J_{\mathrm{out}} = \cos^2[\phi(r)/2], \tag{3}$$

where † indicates the Hermitian complex-conjugate vector.

A MATLAB code was designed to transform the phase signal into a monotonically increasing sequence to unwrap the phase. This is achieved by initialising a new array of the same length as the phase signal, with the first element identical to the phase signal. A loop is then executed that traverses each element of the phase signal, starting from the second element. Within this loop, the absolute value of the derivative of the phase signal at the previous index is computed and added to the previous element of the new array. This process is repeated for all elements in the phase signal, resulting in a new signal that is monotonically increasing, regardless of the behaviour of the original signal. The results are shown in Fig. 6(e)–(h). The phase profiles corresponding to negative topological charges are inverted and plotted in red. The obtained phase shifts are approximated to a linear fit (black line), demonstrating the low deviation from the ideal response. The minimum coefficient of determination is $R^2 = 0.989$, and the maximum $R^2 = 0.995$.

The non-linearity issues, primarily observed in $l = 1$ and 2, are caused by the manufacturing process of the sample. Geometrical deformations in thickness cause an improper distribution, resulting in changes up to $\pi/2$ across the entire area. The maximum observed topological charge is 8, but as 1 V_{RMS} is required, the birefringence curve is non-linear, producing undesired effects in the phase profile. Moreover, the inverted voltage is going to produce a different phase profile. To solve this issue and reach higher values of the topological charge, a LC with a more linear birefringence curve will be required. Also, using a higher birefringence LC can solve this, but higher resolution lithography will be required to minimise the size of the central hole and the gaps between slices.

Insight into the topological charge of an optical vortex can be extracted from its point spread function (PSF), which is the impulse response of a focused optical system, meaning that it reveals how the light intensity is distributed at the focal spot. Fig. 7 presents the PSF at various voltages for a wavelength of 632.8 nm. These results demonstrate that the topological charge can be controlled with precision. A slight variation of the voltage allows eight different topological charges to be achieved. As demonstrated before, the negative topological charge can be easily determined by interchanging the voltages at V_1 and V_2.

It is important to note that while the birefringence of the 6CHBT LC utilised in our study is 0.16, there are other LC materials available, such as TL296 ($\Delta n = 0.215$ at 546 nm) [58] or NLC1929 ($\Delta n = 0.3375$ at 636 nm) [59], which offer higher birefringence values. By utilising such alternative LC materials, the birefringence of the ASPP can be easily doubled, thereby doubling the number of possible topological charges achievable by the device. Furthermore, it is worth mentioning that increasing the thickness of the LC layer directly affects the phase shift produced by the ASPP. As the thickness of the LC layer is increased, the phase shift experienced by the incident light also increases proportionally. Consequently, this leads to an increase in the achievable topological charges by the ASPP. By further increasing the thickness of the LC layer, we can effectively enhance the phase shift and, consequently, expand the range of attainable topological charges

Finally, the setup for conversion efficiency measurements was similar to the one used in Fig. 4. The difference, however, was the exchange of the CMOS2 camera for a photodetector (PD). The pipeline for measurement included detecting the light intensity without the ASPP, with ASPP without voltage powering of the sample and with applied voltages that transfer to the generation of topological charges ±4. The conversion efficiency is calculated through Eq. (4), which is the percentage ratio between the output power with voltage applied with respect to the output power without voltage applied [60].

$$Eff_l = \frac{V_{PD}(Q_l)}{V_{PD}(ASPP_{Off})} \cdot 100\% \tag{4}$$

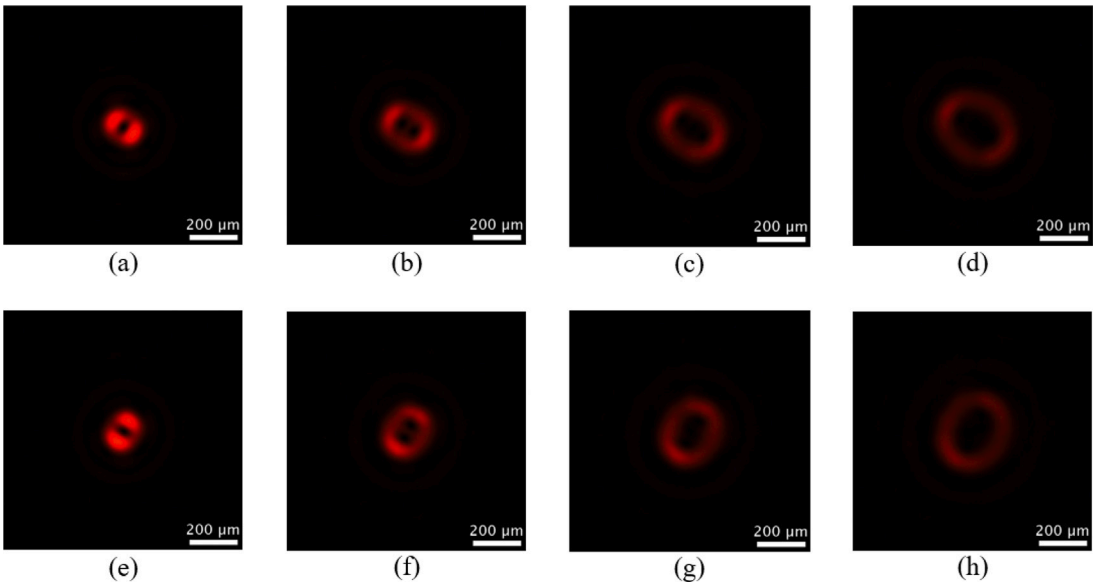

Fig. 7. Focal spot for different topological charges (a) $l = 1$, $V_1 = 1.6$ V_{RMS}, $V_2 = 1.46$ V_{RMS}, (b) $l = 2$, $V_1 = 1.6$ V_{RMS}, $V_2 = 1.34$ V_{RMS}, (c) $l = 3$, $V_1 = 1.61$ V_{RMS}, $V_2 = 1.24$ V_{RMS}, (d) $l = 4$, $V_1 = 1.61$ V_{RMS}, $V_2 = 1.14$ V_{RMS}. (e)–(h) For $l = -1$ to $l = -4$ the inverted voltages in V_1 and V_2 are applied.

Table 1
Measured voltages at the photodiode for different topological charges.

	V_{PD} (mV)	Conversion efficiency (%)
Free path	881.25	
$ASPP_{Off}$	743.75	
Q1	743.75	100.00
Q2	725.00	97.48
Q3	712.50	95.80
Q4	706.25	94.96
-Q1	743.75	100.00
-Q2	732.00	98.42
-Q3	706.25	94.96
-Q4	706.25	94.96

As can be observed in Table 1, almost 100% of conversion efficiency is obtained for topological charge 1. It has to be considered that the PD resolution is 6.25 mV (~0.9%), so this value will be between 99.1% and 100%. Higher topological charges, such as Q4, often exhibit a lower efficiency of conversion (around 95%) compared to lower topological charges like Q1. This discrepancy can be attributed to the complexity of phase profiles associated with higher-order topological charges. These intricate phase profiles are characterised by abrupt variations and defects due to the increased applied voltage and the gaps between pie slices, which can induce scattering or diffraction phenomena, thereby leading to efficiency losses. On the other hand, the transmittance of the cell can be calculated as the percentage ratio between the output power without voltage (Table 1 "$ASPP_{Off}$") and the applied input laser power ("Free Path"). In this case, a transmittance of 84.3% is obtained.

4. Conclusions

In summary, a novel optical vortex generator was proposed and experimentally demonstrated. Using this kind of ASPP, high-quality optical vortices with topological charges from $l = \pm 1$ to ± 4 can be generated by only one ASPP. Due to the continuous optical phase shift, this device has high conversion efficiencies, between 95% to 100% for higher and lower topological charges, respectively. Moreover, the device is entirely reconfigurable (operating wavelengths and topological charges are tunable). The fabrication process is quite similar to that of a normal LCD cell, so it is low-cost and reliable. The device can be used in new applications (e.g., fibre optics communications or atom manipulation) to reduce the fabrication costs of existing devices and generate different topological charges with improved light efficiency, simplicity, and the possibility of reconfiguration.

CRediT authorship contribution statement

T. Jankowski: Investigation. **N. Bennis:** Supervision, Investigation. **P. Morawiak:** Investigation, Fabrication. **D.C. Zografopoulos:** Investigation. **A. Pakuła:** Investigation. **M. Filipiak:** Fabrication. **M. Słowikowski:** Fabrication. **J.M. López-Higuera:** Supervision. **J.F. Algorri:** Supervision, Investigation, Conceptualization.

Declaration of competing interest

The authors declare no conflicts of interest.

Data availability

Data will be made available on request.

Acknowledgements

J. F. Algorri acknowledges the support of the project RYC2022-035279-I funded by MCIN/AEI/10.13039/501100011033 and FSE+. Also, by projects TED2021-130378B-C21 and PID2022-137269OB-C22 funded by MCIN/AEI/10.13039/501100011033/ and by FEDER "A way to make Europe". N. Bennis also acknowledges research project UGB 22-725 (Military University of Technology).

References

[1] J. Hamazaki, R. Morita, K. Chujo, Y. Kobayashi, S. Tanda, T. Omatsu, Optical-vortex laser ablation, Opt. Express 18 (3) (2010) 2144–2151.
[2] K. Toyoda, K. Miyamoto, N. Aoki, R. Morita, T. Omatsu, Using optical vortex to control the chirality of twisted metal nanostructures, Nano Lett. 12 (7) (2012) 3645–3649.
[3] T. Omatsu, K. Miyamoto, K. Toyoda, R. Morita, Y. Arita, K. Dholakia, A new twist for materials science: The formation of chiral structures using the angular momentum of light takashige, Adv. Opt. Mater. 7 (14) (2019) 1801672.
[4] M. Padgett, R. Bowman, Tweezers with a twist, Nat. Photon. 5 (6) (2011) 343–348, http://dx.doi.org/10.1038/nphoton.2011.81.

[5] K. Ladavac, D.G. Grier, Microoptomechanical pumps assembled and driven by holographic optical vortex arrays, Opt. Express 12 (6) (2004) 1144, http://dx.doi.org/10.1364/OPEX.12.001144, URL http://www.opticsexpress.org/abstract.cfm?URI=oe-12-6-1144.

[6] J.W.R. Tabosa, D.V. Petrov, Optical pumping of orbital angular momentum of light in cold cesium atoms, Phys. Rev. Lett. 83 (24) (1999) 4967–4970, http://dx.doi.org/10.1103/PhysRevLett.83.4967, URL http://link.aps.org/doi/10.1103/PhysRevLett.83.4967.

[7] J. Wang, J.-Y. Yang, I.M. Fazal, N. Ahmed, Y. Yan, H. Huang, Y. Ren, Y. Yue, S. Dolinar, M. Tur, A.E. Willner, Terabit free-space data transmission employing orbital angular momentum multiplexing, Nat. Photon. 6 (7) (2012) 488–496, http://dx.doi.org/10.1038/nphoton.2012.138.

[8] N. Bozinovic, Y. Yue, Y. Ren, M. Tur, P. Kristensen, H. Huang, A.E. Willner, S. Ramachandran, Terabit-scale orbital angular momentum mode division multiplexing in fibers, Science 340 (6140) (2013) 1545–1548, http://dx.doi.org/10.1126/science.1237861, URL http://www.sciencemag.org/content/340/6140/1545.

[9] R. Fickler, G. Campbell, B. Buchler, P.K. Lam, A. Zeilinger, Quantum entanglement of angular momentum states with quantum numbers up to 10,010, Proc. Natl. Acad. Sci. USA 113 (2016) 13642–13647.

[10] R.C. Devlin, A. Ambrosio, N.A. Rubin, J.P.B. Mueller, F. Capasso, Arbitrary spin-to–orbital angular momentum conversion of light, Science 358 (2017) 896–901.

[11] T. Stav, A. Faerman, E. Maguid, D. Oren, V. Kleiner, E. Hasman, M. Segev, Quantum entanglement of the spin and orbital angular momentum of photons using metamaterials, Science 361 (2018) 1101–1104.

[12] F. Kong, C. Zhang, F. Bouchard, Z. Li, G.G. Brown, D.H. Ko, T.J. Hammond, L. Arissian, R.W. Boyd, E. Karimi, P.B. Corkum, Controlling the orbital angular momentum of high harmonic vortices, Nature Commun. 8 (2017) 14970.

[13] D. Gauthier, P.R. Ribič, G. Adhikary, A. Camper, C. Chappuis, R. Cucini, L.F. DiMauro, G. Dovillaire, F. Frassetto, R. Géneaux, P. Miotti, L. Poletto, B. Ressel, C. Spezzani, M. Stupar, T. Ruchon, G.D. Ninno, Tunable orbital angular momentum in high-harmonic generation, Nature Commun. 8 (2017) 14971.

[14] J.C.T. Lee, S.J. Alexander, S.D. Kevan, S. Roy, B.J. McMorran, Laguerre–Gauss and Hermite–Gauss soft x-ray states generated using diffractive optics, Nat. Photon. 13 (2019) 205–209.

[15] Z. Xie, T. Lei, F. Li, H. Qiu, Z. Zhang, H. Wang, C. Min, L. Du, Z. Li, X. Yuan, Ultra-broadband on-chip twisted light emitter for optical communications, Light Sci. Appl. 7 (2018) 18001.

[16] N.C. Zambon, P. St-Jean, M. Milićević, A. Lemaître, A. Harouri, L.L. Gratiet, O. Bleu, D.D. Solnyshkov, G. Malpuech, I. Sagnes, S. Ravets, A. Amo, J. Bloch, Optically controlling the emission chirality of microlasers, Nat. Photon. 13 (2019) 283–288.

[17] L. Rego, K.M. Dorney, N.J. Brooks, Q.L.N. Chen Ting Liao, J.S. Román, D.E. Couch, A. Liu, E. Pisanty, C. Hernández-García, Generation of extreme-ultraviolet beams with time-varying orbital angular momentum, Science 364 (6447) (2019).

[18] H.H. Fan, Y.P. Tai, H.H. Li, X.Z. Li, Q.W. Zhan, Epicycle-model-guided arbitrary shaped customization of structured light, Appl. Phys. Lett. 122 (23) (2023) 231104, http://dx.doi.org/10.1063/5.0147002.

[19] L. Zhu, Y. Tai, H. Li, H. Hu, X. Li, Y. Cai, Y. Shen, Multidimensional optical tweezers synthetized by rigid-body emulated structured light, Photon. Res. 11 (9) (2023) 1524–1534, http://dx.doi.org/10.1364/PRJ.490103.

[20] M.A. Geday, M. Caño-García, J.M. Otón, X. Quintana, Adaptive spiral diffractive lenses—lenses with a twist, Adv. Opt. Mater. 8 (23) (2020) 2001199, http://dx.doi.org/10.1002/adom.202001199.

[21] K. i. Yuyama, H. Kawaguchi, R. Wei, T. Omatsu, Fabrication of an array of hemispherical microlasers using optical vortex laser-induced forward transfer, ACS Photon. (2023) http://dx.doi.org/10.1021/acsphotonics.3c01005.

[22] M.W. Beijersbergen, R.P.C. Coerwinkel, M. Kristensen, J.P. Woerdman, Helical-wavefront laser beams produced with a spiral phaseplate, Opt. Commun. 112 (6) (1994) 321–327.

[23] N.R. Heckenberg, R. McDuff, C.P. Smith, A.G. White, Generation of optical phase singularities by computer-generated holograms, Opt. Lett. 17 (3) (1992) 221, http://dx.doi.org/10.1364/OL.17.000221, URL http://ol.osa.org/abstract.cfm?URI=ol-17-3-221.

[24] X. Wang, Z. Nie, Y. Liang, J. Wang, T. Li, B. Jia, Recent advances on optical vortex generation, Nanophotonics 7 (9) (2018) 1533–1556, http://dx.doi.org/10.1515/nanoph-2018-0072.

[25] I. Zeylikovich, H.I. Sztul, V. Kartazaev, T. Le, R.R. Alfano, Ultrashort Laguerre-Gaussian pulses with angular and group velocity dispersion compensation, Opt. Lett. 32 (14) (2007) 2025, http://dx.doi.org/10.1364/OL.32.002025, URL http://ol.osa.org/abstract.cfm?URI=ol-32-14-2025.

[26] K. Crabtree, J.A. Davis, I. Moreno, Optical processing with vortex-producing lenses, Appl. Opt. 43 (6) (2004) 1360, http://dx.doi.org/10.1364/AO.43.001360, URL http://ao.osa.org/abstract.cfm?URI=ao-43-6-1360.

[27] A. Forbes, A. Dudley, M. McLaren, Creation and detection of optical modes with spatial light modulators, Adv. Opt. Photon. 8 (2) (2016) 200.

[28] J.M.O. Sanchez, J. Pereiro-García, X. Quintana, M. Caño-García, E. Otón, M.A. Geday, Optimizing tunable lc devices with twisted light, 2023, http://dx.doi.org/10.20944/preprints202311.0668.v1, Preprints.

[29] D. Ganic, X. Gan, M. Gu, M. Hain, S. Somalingam, S. Stankovic, T. Tschudi, Generation of doughnut laser beams by use of a liquid-crystal cell with a conversion efficiency near 100%, Opt. Lett. 27 (15) (2002) 1351–1353, http://dx.doi.org/10.1364/OL.27.001351.

[30] B. Wang, M. Ye, S. Sato, Lens of electrically controllable focal length made by a glass lens and liquid-crystal layers, Appl. Opt. 43 (17) (2004) 3420–3425, URL http://www.opticsinfobase.org/abstract.cfm?&id=80172.

[31] J. Albero, P. Garcia-Martinez, N. Bennis, E. Oton, B. Cerrolaza, I. Moreno, J.A. Davis, Liquid crystal devices for the reconfigurable generation of optical vortices, J. Lightwave Technol. 30 (18) (2012) 3055–3060.

[32] M. Caño-García, X. Quintana, J.M. Otón, M.A. Geday, Dynamic multilevel spiral phase plate generator, Sci. Rep. 8 (1) (2018) 15804, http://dx.doi.org/10.1038/s41598-018-34041-2.

[33] J. Pereiro-García, M. García-de Blas, M. Geday, et al., Flat variable liquid crystal diffractive spiral axicon enabling perfect vortex beams generation, Sci. Rep. 13 (2023) 2385, http://dx.doi.org/10.1038/s41598-023-29164-0.

[34] R.C. Devlin, A. Ambrosio, D. Wintz, S.L. Oscurato, A.Y. Zhu, M. Khorasaninejad, J. Oh, P. Maddalena, F. Capasso, Spin-to-orbital angular momentum conversion in dielectric metasurfaces, Opt. Express 25 (1) (2017) 377–393, http://dx.doi.org/10.1364/OE.25.000377.

[35] K.E. Chong, I. Staude, A. James, J. Dominguez, S. Liu, S. Campione, G.S. Subramania, T.S. Luk, M. Decker, D.N. Neshev, I. Brener, Y.S. Kivshar, Polarization-independent silicon metadevices for efficient optical wavefront control, Nano Lett. 15 (8) (2015) 5369–5374, http://dx.doi.org/10.1021/acs.nanolett.5b01752.

[36] R. Collier, Optical Holography, Elsevier Science, 2013, URL https://books.google.es/books?id=pCmlsUKAU8wC.

[37] P. Chen, B.-Y. Wei, W. Ji, S.-J. Ge, W. Hu, F. Xu, V. Chigrinov, Y.-Q. Lu, Arbitrary and reconfigurable optical vortex generation: a high-efficiency technique using director-varying liquid crystal fork gratings, Photon. Res. 3 (4) (2015) 133–139, http://dx.doi.org/10.1364/PRJ.3.000133, URL https://opg.optica.org/prj/abstract.cfm?URI=prj-3-4-133.

[38] Z. Guo, S. Qu, S. Liu, Generating optical vortex with computer-generated hologram fabricated inside glass by femtosecond laser pulses, Opt. Commun. 273 (1) (2007) 286–289, http://dx.doi.org/10.1016/j.optcom.2006.12.023.

[39] Y.J. Liu, X.W. Sun, Q. Wang, D. Luo, Electrically switchable optical vortex generated by a computer-generated hologram recorded in polymer-dispersed liquid crystals, Opt. Express 15 (25) (2007) 16645–16650, http://dx.doi.org/10.1364/OE.15.016645.

[40] Y.J. Liu, X.W. Sun, D. Luo, Z. Raszewski, Generating electrically tunable optical vortices by a liquid crystal cell with patterned electrode, Appl. Phys. Lett. 92 (10) (2008) 101114, http://dx.doi.org/10.1063/1.2894521.

[41] S.-J. Ge, W. Ji, G.-X. Cui, B.-Y. Wei, W. Hu, Y.-Q. Lu, Fast switchable optical vortex generator based on blue phase liquid crystal fork grating, Opt. Mater. Express 4 (12) (2014) 2535–2541, http://dx.doi.org/10.1364/OME.4.002535, URL https://opg.optica.org/ome/abstract.cfm?URI=ome-4-12-2535.

[42] B.-y. Wei, W. Hu, Y. Ming, F. Xu, S. Rubin, J.-g. Wang, V. Chigrinov, Y.-q. Lu, Generating switchable and reconfigurable optical vortices via photopatterning of liquid crystals, Adv. Mater. 26 (10) (2014) 1590–1595, http://dx.doi.org/10.1002/adma.201305198.

[43] J.F. Algorri, D. Zografopoulos, A. Spadlo, L. Rodríguez-cobo, L.R. Jaroszewicz, J.M. Sánchez-pena, J.M. López-Higuera, Multifunctional light beam control device by stimuli-responsive liquid crystal micro-grating structures, Sci. Rep. 10 (2020) 13806, http://dx.doi.org/10.1038/s41598-020-70783-8.

[44] Z. Zemska, T. Galstian, Simple electrically tunable liquid crystal spatial phase modulator, Opt. Express 31 (4) (2023) 5388–5398, http://dx.doi.org/10.1364/OE.483736.

[45] J.F. Algorri, P. Morawiak, D.C. Zografopoulos, N. Bennis, A. Spadlo, L. Rodriguez-Cobo, L.R. Jaroszewicz, J.M. Sanchez-Pena, J.M. Lopez-Higuera, Cylindrical and Powell liquid crystal lenses with positive-negative optical power, IEEE Photonics Technol. Lett. 32 (17) (2020) 1057–1060, http://dx.doi.org/10.1109/lpt.2020.3011673.

[46] W. Feng, Z. Liu, M. Ye, Positive-negative tunable cylindrical liquid crystal lenses, Optik 266 (2022) 169613, http://dx.doi.org/10.1016/j.ijleo.2022.169613.

[47] J.F. Algorri, P. Morawiak, N. Bennis, D.C. Zografopoulos, V. Urruchi, L. Rodríguez-Cobo, L.R. Jaroszewicz, J.M. Sánchez-Pena, J.M. López-Higuera, Positive-negative tunable liquid crystal lenses based on a microstructured transmission line, Sci. Rep. 10 (1) (2020) 10153, http://dx.doi.org/10.1038/s41598-020-67141-z.

[48] J. Stevens, T. Galstian, Electrically tunable liquid crystal lens with a serpentine electrode design, Opt. Lett. 47 (4) (2022) 910–912, http://dx.doi.org/10.1364/OL.447853, URL http://opg.optica.org/ol/abstract.cfm?URI=ol-47-4-910.

[49] N. Bennis, T. Jankowski, P. Morawiak, A. Spadlo, D.C. Zografopoulos, J.M. Sánchez-Pena, J.M. López-Higuera, J.F. Algorri, Aspherical liquid crystal lenses based on a variable transmission electrode, Opt. Express 30 (8) (2022) 12237–12247, http://dx.doi.org/10.1364/OE.451292, URL http://opg.optica.org/oe/abstract.cfm?URI=oe-30-8-12237.

[50] J.F. Algorri, D.C. Zografopoulos, L. Rodríguez-Cobo, J.M. Sánchez-Pena, J.M. López-Higuera, Engineering aspheric liquid crystal lenses by using the transmission electrode technique, Crystals 10 (9) (2020) 835, http://dx.doi.org/10.3390/CRYST10090835, URL https://www.mdpi.com/2073-4352/10/9/835/htmhttps://www.mdpi.com/2073-4352/10/9/835.

[51] A. Pusenkova, O. Sova, T. Galstian, Electrically variable liquid crystal lens with spiral electrode, Opt. Commun. 508 (2022) 127783, http://dx.doi.org/10.1016/j.optcom.2021.127783, URL https://www.sciencedirect.com/science/article/pii/S0030401821009585.

[52] W. Feng, Z. Liu, H. Liu, M. Ye, Design of tunable liquid crystal lenses with a parabolic phase profile, Crystals 13 (1) (2023) http://dx.doi.org/10.3390/cryst13010008.

[53] W. Feng, Z. Liu, M. Ye, Liquid crystal lens with a shiftable optical axis, Opt. Express 31 (10) (2023) 15523–15536, http://dx.doi.org/10.1364/OE.488844.

[54] W. Feng, Z. Liu, M. Ye, Liquid crystal lens array with positive and negative focal lengths, Opt. Express 30 (16) (2022) 28941–28953, http://dx.doi.org/10.1364/OE.464526.

[55] R. Dabrowski, J. Dziaduszek, T. Szczucinski, 4-/trans-4'-n-alkylcyclohexzyl/isothiocyanatobenzenes a new class of low-melting stable nematics, Mol. Cryst. Liq. Cryst. 102 (Lett 5) (1984) 155–160, http://dx.doi.org/10.1080/01406568408072065.

[56] R. Buchecker, M. Schadt, Synthesis, physical properties and structural relationships of new, end-chain substituted nematic liquid crystals, Mol. Cryst. Liq. Cryst. 149 (1) (1987) 359–373, http://dx.doi.org/10.1080/00268948708082991.

[57] J.F. Algorri, V. Urruchi Del Pozo, P. Pinzón, J.M. Sánchez Pena, Modeling electro-optical response of nematic liquid crystals by numerical methods, Opt. Apl. 46 (4) (2013) 327–336, http://dx.doi.org/10.7149/OPA.46.4.327, URL http://dialnet.unirioja.es/servlet/articulo?codigo=4538743&info=resumen&idioma=SPA.

[58] J.F. Algorri, B. Garcia-Camara, A. Garcia-Garcia, V. Urruchi, J.M. Sánchez-Pena, Fiber optic temperature sensor based on amplitude modulation of metallic and semiconductor nanoparticles in a liquid crystal mixture, J. Lightwave Technol. 33 (12) (2015) 2451–2455, http://dx.doi.org/10.1109/JLT.2015.2396357, URL http://ieeexplore.ieee.org/lpdocs/epic03/wrapper.htm?arnumber=7042741.

[59] N. Bennis, T. Jankowski, O. Strzezysz, A. Pakuła, D.C. Zografopoulos, P. Perkowski, J.M. Sánchez-Pena, J.M. López-Higuera, J.F. Algorri, A high birefringence liquid crystal for lenses with large aperture, Sci. Rep. 12 (1) (2022) 14603, http://dx.doi.org/10.1038/s41598-022-18530-z.

[60] Q. Wang, X.W. Sun, P. Shum, Generating doughnut-shaped beams with large charge numbers by use of liquid-crystal spiral phase plates, Appl. Opt. 43 (11) (2004) 2292–2297, http://dx.doi.org/10.1364/AO.43.002292.